Article

Not peer-reviewed version

Pressure-Induced Graphene-like Si Layer in Ductile RuSi2 with Ambient-Pressure Superconductivity and High Hardness

Chuanzhao Zhang , Yanqi Wang , Mengqiu Li , Fulong Yang , Kaixiong Gao , Yuanyuan Jin * , Weiguo Sun *

Posted Date: 7 October 2024

doi: 10.20944/preprints202410.0466.v1

Keywords: transition metal disilicide; 2D silicon layer; first principles; electronic property; superconductivity; hardness

 doi:10.20944/preprints202410.0466.v1

Article

Pressure-Induced Graphene-like Si Layer in Ductile $RuSi_2$ with Ambient-Pressure Superconductivity and High Hardness

Chuanzhao Zhang [1], Yanqi Wang [1], Mengqiu Li [1], Fulong Yang [1], Kaixiong Gao [2], Yuanyuan Jin [1,*] and Weiguo Sun [3,*]

[1] Department of Physics and Optoelectronic Engineering, Yangtze University, Jingzhou 434023, China
[2] State Key Laboratory of Solid Lubrication, Lanzhou Institute of Chemical Physics, Chinese Academy of Sciences, Lanzhou 730000, China
[3] College of Physics and Electronic Information, Luoyang Normal University, Luoyang 471022, China
* Correspondence: scujyy@163.com (Y.J); xwswguo@163.com (W.S)

Abstract: Of particular interest is the serendipity of distinctive nonmetallic layered frameworks with the stoichiometry of 1:2 in the binary metallic compounds within inorganic chemistry and materials science. This not only gives rise to the unexpected properties, especially the distinguished superconductivity, as reflected in MgB_2, MoB_2, NaC_2, LaP_2 and CeP_2, but also strengthens the cognition of the elemental contributions. Although various investigations on the superconducting performances in the alkali, alkaline-earth and rare-earth metal disilicides containing the silicon layers have been reported, the pursuit of superconductors with silicon-planar framework in transition metal disilicides remain unknown up to now. In the present work, crystal structure searches and first-principles calculations were thoroughly conducted in $RuSi_2$ within the pressure range of 0-300 GPa to uncover the novel structures, incredible silicon building block and the amazing properties. The ground orthorhombic *Cmca*-$RuSi_2$ phase at ambient pressure is a semiconductor with the band gap of 0.485 eV, whose hardness can reach 31.7 GPa. Even more intriguingly, the high-pressure orthorhombic *Cmcm*-$RuSi_2$ configuration with the fabulous graphene-like silicon-layer, which can be theoretically stabilized with the transformation pressure of 50.97 GPa, can be unexpectedly recovered to ambient pressure. Electron-phonon coupling calculations unravels that it possesses the metallic trait with an estimated T_c value of 1.43 K at 75 GPa, which increases to 10.07 K under ambient pressure. The enhanced T_c stems from the increased density of states at the Fermi level and associated with the coupled vibrations between Ru and the planar Si layer. Meanwhile, the hardness value for *Cmcm*-$RuSi_2$ is 26.8 GPa under ambient pressure, which further results from the three-dimensional covalent Ru-Si and Si-Si building blocks. The coexistence of superconductivity and high hardness in the *Cmcm*-$RuSi_2$ configuration under ambient pressure will pave the way for delving into more binary transition-metal silicides and correlated ternary silicides with the profound silicon layers.

Keywords: transition metal disilicide; 2D silicon layer; first principles; electronic property; superconductivity; hardness

Introduction

Last decade has witnessed the exuberant development of superconductor, which discloses a variety of advanced superconductor materials. Among these superconductors, a class of binary compound constituted by rich nonmetallic and metallic elements has garnered climbing interest from academic and industrial communities not only due to the considerable superconducting transition temperature T_c but also owing to the unprecedented nonmetallic polymetric configurations. In the binary hydride superconductors, the special H_{24}, H_{29}, H_{32} and H_{36} clathrate structures were verified in CaH_6 [1,2], YH_9 [3,4], LaH_{10} [5,6] and CeH_{18} [7] with the near or even above room-temperature T_c values of 205 K (172 GPa), 262 K (182 GPa), 250 K (170 GPa), and 329 K (350 GPa), respectively. Recently, another A-15 type structure of *Pm*-3*n*-Lu_4H_{23} [8] was further proposed with a measured T_c value of 71 K (218 GPa), which consists of a combined clathrate structure of H_{20} and H_{24} cage. This

 doi:10.20944/preprints202410.0466.v1

idea stems from the Si clathrate structures in Ba_8Si_{46} [9,10] with the low-temperature properties. The high temperature T_cs in these hydrogen clathrate structures are closely associated with sodalite H clathrate structure, because the stretching and rocking vibrations of H atoms within H-cage contribute to strong electron-phonon coupling. Apart from the three dimensional (3D) hydrogen cage structure in the binary hydrogen-rich superconductor, two unpredictable hydrogen configurations with high T_cs enter into the scientists' horizon, which not only contains one-dimensional (1D) nanotubes in HfH_9 (110 K, 200 GPa) [11] and H_7 chains in GaH_7 (~100 K, 200–300 GPa) [12], but also consists of the momentous two-dimensional (2D) layered configurations. These 2D layered structures can be typified by the wavy H layer containing the edge-sharing pea-like H_{18} ring in LiH_4 (93.6 K, 100 GPa) [13], exotic layered structure composed of quasimolecular H_2 and linear H_3 units in KH_6 (58.6–69.8 K, 166 GPa) [14], puckered hexagonal honeycomb of H atoms sandwiched between slabs of atomic Fe and H atoms in FeH_5 (51 K, 130 GPa) [15], hydrogen pentagraphenelike structure in HfH_{10} (213–234 K, 250 GPa) [16] and H_9 nonagon in XH_{15} (X = Ca, Sr, Y and La) [17] with the estimated high T_c values of 189 K at 200 GPa, 139 K at 300 GPa, 208 K at 220 GPa and 113 K at 200 GPa, respectively. Although the breakthroughs in achieving high transition temperature T_c have breathed new life into the pursuit of room-temperature superconductivity, the extremely high pressures (usually surpassing 100 GPa) in synthesizing these hydride-based superconductors involving diamond anvil cell (DAC) necessitates the use of culet with the small sample size ranging from 40 to 80 μm [18]. Nevertheless, the small sample size conduces to the weak magnetic measurements challenging and makes precise temperature control difficult. On the other hand, the DAC for the synthesis were always broken during depressurization owing to the hydrogen embrittlement [19,20]. Both aspects are expected to get rid of the hydride superconductor under high pressure, which portends the advent of other non-H building blocks in binary metal compounds under lower or even atmospheric pressures.

In the binary compounds containing metal and non-H light element (B, C, N and P), a variety of researchers endeavored to dig into their superconductivity and extraordinary nonmetallic frameworks, especially for 2D planar motifs. The planar nonmetallic skeleton is of great interest due to the spectacular properties, such as distinct superconductivity. Starting from metal borides, MgB_2 (at 1atm) [21] and MoB_2 (under 100 GPa) [22] within the identical *P6/mmm* symmetry possess the highest and second highest T_cs of corresponding 39 and 32 K because of the 2D graphitic boron layer among the metal borides. In the metal carbides, the predicted superconducting critical temperature T_c for NaC_2 [23] could approach ~42 K at 80 GPa with the existence of hexagonal rings, which is slightly higher that of MgB_2 [21]. Moreover, YC_2 was also theoretically verified to be a good superconductor with the estimated T_c value of 2.9 K [24], characterized by the 2D graphite sheet. Importantly, the KN_2 [25] monolayer presents a unique superconducting trait with an estimated critical temperature (T_c) of 4.3 K under ambient condition. Furthermore, the particular novel planar N_4 unit gives rise to the phonon-mediated superconductivity with the T_c value of 4–8 K in *P6*$_3$*/mcm*-FeN_2 [26]. Last but not least, the *I*4*/mmm*-KP_2 [27] configuration with puckered phosphorus layer is predicted to have the superconducting critical temperature T_c of 22 K under 5 GPa. Moreover, the calculated T_c values for CeP_2 [28] under ambient pressure (T_c = 30.77 K) and LaP_2 [29] at 11 GPa (T_c = 22.2 K), regarded as the the highest and second highest T_cs among those of already known binary transition-metal phosphorus, which should be attributed to the graphene-like P layer. From the anterior discussions, two recognizable traits for these binary metal compounds with superb superconductivity fade into our sight, the stoichiometry of 1: 2 and the nonmetallic layered framework (B, C, N and P). In consequence, to uncover more marvelous superconductors, we need to achieve more fresh structures containing the nonmetallic layer fabrications in this category of compounds.

Surrounded by B, C, N and P elements in the periodic table of elements, Si is a common but useful element for a great number of fields, such as integrated circuits and solar cells. Contrary to the semiconductor properties of silicon at ambient pressure, the metal silicides possess the superconducting properties in consequence of its various intriguing motifs (e.g. 3D cages and 2D buckled layers). In the 3D silicon cage system, Ba_8Si_{46} [30] consists of a combination of Si_{20} and Si_{24}

 doi:10.20944/preprints202410.0466.v1

cages linked by sharing a pentagonal face with the estimated T_c of 8 K at ambient pressure while $Ba_{24}Si_{100}$ [31] contains Si_{20} cage with the T_c value of 1.4 K at the pressure of 1.5 GPa. Subsequent experiment proposed that $LaSi_{10}$ [32] is deemed as a superconductor with T_c = 6.7 K. Moreover, the superconducting critical temperature of *P*6/*m*-$NaSi_6$ [33] is estimated to be 13.1 K with the silicon clathrate configuration, in which all Si atoms form simple hexagonal open channels and guest Na atoms fill the channels. Apart from the 3D silicon clathrate configurations, another extraordinary example of graphite-like 2D-structured sub-network are metal disilicides in the form of MSi_2, where M represents the metal atom. This kind compound is very stable and multifunctional and can be chemically modified by oxidation, which further could induce novel silicon framework such as layered silicon, silicon clathrates and other silicon allotropes after removing the metals. More interestingly, the superconducting phenomenon can be achieved in such layered silicides, which hence stimulate the experimental and theoretical discoveries of the interesting superconductivity in MSi_2. In the alkali-metal disilicides, $RbSi_2$ [34] with the trigonal $EuGe_2$-type phase (space group: *P*-3*m*1, 164), characterized by the hexagonal honeycomb structure, was predicted to have the T_c value of 9 K. For the alkaline-earth metal disilicides, three layered phases in $MgSi_2$ [35,36] namely, the *R*-3*m* phase at 0 GPa, *Imma* phase at 10 GPa and *P*6/*mmm* phase at 20 GPa were predicted to possess the superconducting critical temperature T_c values of ~7, ~6.9 and ~7 K, respectively. $CaSi_2$ [37,38] is transformed to the hexagonal AlB_2-type structure (space group: *P*6/*mmm*, 191) with the graphite-like Si layers at 15 GPa in experiment, which displays a superconducting transition at 14 K. Moreover, the high pressure of $BaSi_2$ [39] with the $EuGe_2$-type layered configuration is a superconductor with the experimentally measured T_c value of 6.8 K. In rare-earth metal disilicides, $LaSi_2$ [40] is considered as a superconductor with the tetragonal $ThSi_2$-type (*I*4$_1$/*amd*, 141) layered structure, which has the superconducting T_c value of 2.5 K. Recently, another theoretical group studied the superconductivity of the binary Y–Si system and pointed out that the estimated T_c value of *Imma*-YSi_2 [41] with the apparent layered structure is 0.5 K at 50 GPa. Based on the anterior superconductivity discussions, the layered structures in metal disilicides MSi_2 cover alkali, alkaline-earth and rare-earth metal disilicides. Nevertheless, a distinct category of metal disilicides, namely, transition metal disilicides may be neglected in previous investigations, which arouses our interest in the quest for the layered structures with exceptional superconductivity in transition-metal disilicides.

Chemical substitution is one of the diverse routes in chemical pressure, which can tune the structures and properties of materials [42,43]. Following on this method, we replace alkali, alkaline-earth and rare-earth metal with the considered transition metal in MSi_2. As is generally known, ruthenium element is located in the VIII group of the periodic table and is a typical transition metal element, which is selected as a representative transition metal. According to the experiment, there are four compounds (e.g., RuSi [44,45], Ru_2Si_3 [45–47], Ru_4Si_3 [45,46] and $RuSi_2$ [48]) in the binary Ru-Si system under atmospheric pressure. Zhang et al. theoretically predicted three stable compounds in the binary Ru-Si system at ambient pressure, namely, RuSi, Ru_2Si_3 and $RuSi_2$ through the CALYPSO crystal structure prediction method in combination with first-principles [49]. Both experiment and theory confirm the stable existence of RuSi, Ru_2Si_3 and $RuSi_2$ in Ru-Si system under ambient pressure, which exhibit the semiconductor characters with narrow band gaps. RuSi consists of two polymorphic types, in other words, the FeSi-type phase with space group of *P*2$_1$3 at low temperature and the CsCl-type phase with space group of *Pm*-3*m* at high temperature [50]. Ru_2Si_3 crystallizes in the orthorhombic *Pbcn* configuration [45–47]. More importantly, $RuSi_2$ was reported experimentally for the first time and analyzed theoretically with three possible phases, tetragonal α-$RuSi_2$ (*P*4/*mmm*), orthorhombic β-$RuSi_2$ (*Cmca*) and cubic γ-$RuSi_2$ (*Fm*-3*m*) [51]. Recently, Zhang et al theoretically confirmed that the component $RuSi_2$ with the *Cmca* phase is stable in the convex hull of the binary Ru–Si system based on the CALYPSO crystal research method and first-principles [49]. However, the exploration on $RuSi_2$ has focused only on the structures and electronic properties under the atmospheric pressure in spite of the fantastic silicon framework and unexpected properties possibly existing under the high pressure condition, for example, the novel structures with superconductivity. High pressure is an effective methodology to induce the structural transition of materials, bringing about the variation of the properties [52,53], for instance, the evolution from insulator or

 doi:10.20944/preprints202410.0466.v1

semiconductor to metallicity or superconductivity. Moreover, RuSi undergoes a structural transition from FeSi-type to CsCl-type cubic structure at 0.28 GPa, accompanied by the semiconductor-metal conversion [50]. These two aspects enhance our confidence in pursuing the novel structures with superconductivity in $RuSi_2$ under high pressure. Impressed by the layered structures with the alkali, alkaline-earth and rare-earth metal disilicides discussed above, two questions has been lingering in my mind. could the novel phases appear for $RuSi_2$ under high pressure? Furthermore, if novel structures could stabilized under high pressure, could the high-pressure phases contain the layered silicon motifs with the superconductivity and superb hardness?

To resolve the aforementioned two problems, we performed an extensive study on the potential $RuSi_2$ configurations over the pressure range of 0–300 GPa by applying an unbiased CALYPSO method combined with first-principles calculations. Herein, we report an absolutely novel $RuSi_2$ configuration with the orthorhombic *Cmcm* symmetry under high pressure, composed of a graphene-like silicon-layer with one centered ruthenium atom. More intriguingly, this configuration can be quenchable after releasing the pressure down to ambient pressure. The *Cmcm*-$RuSi_2$ structure exhibits the superconducting character with the superconducting critical temperature of 10.07 K at ambient pressure, which is the second highest temperature among the MSi_2 (M = metal) silicides (*R*-3*m*-$CaSi_2$, 14 K) [38]. In addition, its Vicker hardness value can reach 26.76 GPa, makes it become a rarely hybrid material that simultaneously behaves the superconducting property and high hardness under atmospheric pressure. This investigation provide a new pathway for the design of hard superconductors in transition-metal silicides, which will arouse the interest of the experimental researchers in synthesizing transition metal disilicides and measuring related properties.

2. Computational Method

The structure searches of $RuSi_2$ materials under high pressure are based on the particle swarm optimization (PSO) algorithm as implemented in the crystal structure prediction CALYPSO code [54,55], which has successfully predicted the ambient-pressure and high-pressure structures of various systems [56-59]. In the pressure range of 0–300 GPa, we implemented the structure searches with unit cells including up to four formula units (f.u.). The structural geometrical optimization, electronic structure, Bader charge, electron localization functions (ELF) [60,61] and elastic constants calculations were performed through density functional theory in the Vienna ab initio simulation package (VASP) [62] within the Perdew–Burke–Ernzerhof (PBE) exchange correlation function of generalized gradient approximation (GGA) [63,64]. The Projector-Augmented Wave (PAW) [65] method was adopted to treat $4d^7 5s^1$ and $3s^2 3p^2$ as valence electrons for Ru and Si atoms, respectively. In addition, the cutoff energy of 800 eV for the plane-wave basis expansion of the electronic wave functions was implemented and appropriate Monkhorst–Pack *k* meshes for sampling in the Brillouin zone were set to ensure that all the enthalpy calculations were well converged to better than 1 meV/atom [66]. The crystal orbital Hamilton population (COHP) method was applied in LOBSTER code [67,68]. The phonon and electron-phonon coupling (EPC) matrix elements were calculated within density functional perturbation theory (DFPT) as implemented in the QUANTUM ESPRESSO package [69] with a kinetic cutoff energy of 80 Ry. In the first Brillouin zone, we have selected *k*-point meshes for *Cmcm*-$RuSi_2$ phase of 12 × 12 × 12 at 1 atm and 10 × 10 × 10 at 25, 50 and 75 GPa, respectively. The *q*-point meshes for *Cmcm*-$RuSi_2$ phase were set to 3 × 3 × 3 at 1 atm and 5 × 5 × 5 at 25, 50 and 75 GPa, respectively.

3. Results and Discussion

3.1. Structural Transition and Dynamical Stability

In the first instance, in order to determine the structural transition sequence and potential stable structures for $RuSi_2$ under high pressure, we carried out the CALYPSO code for thoroughly crystal structure searches. As a result, nine candidate low-energy structures with space groups of *Cmca*, *Cmcm*, *P*2/*m*, *Immm*, *Cm*, $P3_212$, *Imm*2, *C*2 and $P2_1/m$ were predicted at the pressure range of 0–300 GPa. The structural diagrams, together with detailed structural parameters of nine candidate phases

 doi:10.20944/preprints202410.0466.v1

under ambient pressure are summarized in Figure S1 and Table S1 of the Supplementary Information (SI). The previously known *Cmca* [49,70] and *Immm* [71] structures of transition metal disilicide $RuSi_2$ were successfully reproduced by our structure searches, demonstrating the reliability of the CALYPSO method. Subsequently, we constructed the enthalpy-pressure (H–P) curves of the low-energy phases and presented two possible decomposition routes (Ru + 2Si and RuSi + Si) with respect to *Cmca* phase, as shown in Figure 1. The phase stability of $RuSi_2$ compound is established at various pressures by judging the enthalpy difference relative to the solid constituent elements and stable compounds (i.e. Ru, Si solid phase, and RuSi compound). The corresponding known stable elements $P6_3/mmc$ for Ru [72], Fd-3m, $P6_3/mmc$, and Fm-3m for Si [73], and compounds $P2_13$ and Pm-3m for RuSi [44,45,74] under corresponding pressures were achieved from the previous literature. According to Figure 1, $RuSi_2$ adopts the orthorhombic β-$FeSi_2$ type configuration (space group: *Cmca*) as ground-state structure under ambient pressure, which is consistent with the previous experimental observations and theoretical researches [49,51,75]. As the pressure increases, the $RuSi_2$ is found to crystallize in another orthorhombic *Cmcm* phase, which is energetically favored over the *Cmca*-$RuSi_2$ above 50.97 GPa and maintains its stability up to 79.15 GPa. Noticeably, this *Cmcm*-$RuSi_2$ configuration is absolutely distinctive from previously reported metal disilicides MSi_2, such as hexagonal $P6/mmm$-type phase in $MgSi_2$ [35,36] and $CaSi_2$ [37,38], trigonal P-3m1 phase in $RbSi_2$ [34] and alkaline-earth metal disicides, trigonal $I4_1/amd$ phase in $LaSi_2$ [40], rhombohedral R-3m phase in $MgSi_2$ [35,36], and orthorhombic *Imma* in $MgSi_2$ [35,36] and YSi_2 [41] Hence, this orthorhombic *Cmcm* phase is predicted to be a high-pressure ground-state structure in metal disilicides in the present work for the first time. Above 79.15 GPa, the $RuSi_2$ compound decomposes into RuSi + Si. Additionally, the considered pressure dependence of $RuSi_2$ decomposition reaction proves that $RuSi_2$ will not decompose into Ru + 2Si within the pressure range of 0–78.48 GPa (see Figure 1). Thus, compressing RuSi and Si is a potential synthetic route for $RuSi_2$ crystal. The above analysis demonstrates the thermodynamical stability of *Cmca*-$RuSi_2$ and *Cmcm*-$RuSi_2$ phases and provides their potential synthetic routes, which will stimulate the experimental synthesis. Subsequently, we focus on the structural, chemical bonding, electronic, superconducting and mechanical characters for the *Cmca*-$RuSi_2$ and *Cmcm*-$RuSi_2$ phases.

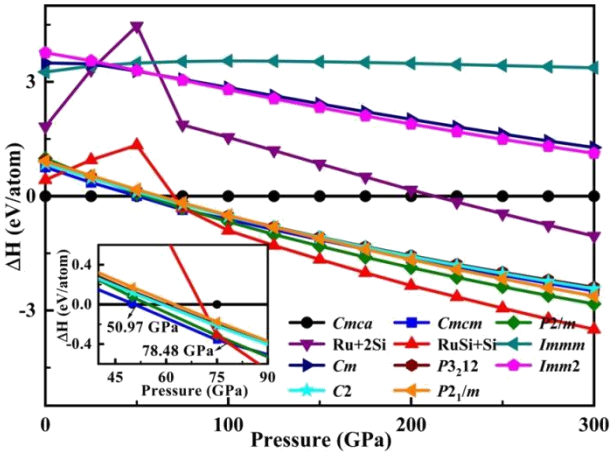

Figure 1. The enthalpy curves for nine low-energy candidate phases and two considered decomposition routes with respect to *Cmca* phase. The inset shows the specific decomposition pressure of $RuSi_2$.

To probe into the dynamical stability of two thermodynamical stable structures under specific pressures, we have computed their phonon dispersion curves (see Figures S2 and 7). It is evidently found that both the *Cmca*-$RuSi_2$ phase at atmospheric pressure and the *Cmcm*-$RuSi_2$ phase at the pressure range of 0–75 GPa are dynamically stable, as there is no imaginary frequency in the whole Brillouin zone. Although the *Cmcm*-$RuSi_2$ structure can be acquired under high pressure, it can be recovered to ambient pressure condition, thereby render it applicable in practical settings.

 doi:10.20944/preprints202410.0466.v1

Subsequently, we mainly focus on the the structural, chemical bonding, electronic, superconducting and mechanical features for the *Cmca*-$RuSi_2$ and *Cmcm*-$RuSi_2$ phases under atmospheric pressure.

3.2. Structural Character and Bonding Essence

The crystal structure diagrams for the *Cmca*-$RuSi_2$ phase at 1 atm and the *Cmcm*-$RuSi_2$ phase at 75 GPa were distinctly depicted in Figure 2 and homologous structural parameters were tabulated in Table S2. From Table S2, the lattice parameters (a = 10.170 Å, b = 8.108 Å, and c = 8.209 Å) of *Cmca*-$RuSi_2$ excellently align with previous results (a = 10.223 Å, b = 8.133 Å, and c = 8.250 Å) [49,51,75]. In this structure, there are two inequivalent Si atoms located at the Wyckoff sites 16*g* (0.372, -0.778, 0.057) and 16*g* (0.127, -0.551, 0.225), respectively, with Si-Si separations varying from 2.54 to 2.62 Å. All the Si atoms form a ladder-like Si-network framework with the planar quadrangle along the b axis and the angle between the nearest three Si atoms is nearly 90°. The shortest Si-Si distance (2.54 Å) is marginally longer than the those of Si (2.22 Å) atoms, *d*-Si (2.35 Å) [76], and allotrope *Cmcm*-Si_{24} (2.33-2.41 Å) [76], but comparable to those of C49-WSi_2 [77] (2.56 Å) and B31-RhSi (2.53-2.69 Å) [78], expounding the contribution of Si-Si covalent bond to the structure construction. This result can be evidenced by the electron localization function (ELF) for the *Cmca*-$RuSi_2$ under ambient pressure, as displayed in Figure 3(a) and 3(b), which precisely describes the electron localization between Si atoms. Besides, each Ru atom is coordinated by eight Si atoms, forming a "$RuSi_8$" building block with Ru-Si separation range of 2.45-2.52 Å. The shortest Ru-Si distance (2.45 Å) is slightly longer than the sum of the covalent bond radii of Ru (1.25 Å) and Si (1.11 Å) atoms, indicating the covalent Ru-Si bond, which can be demonstrated by ELF in Figures 3(a) and 3(b) as well. For the *Cmcm*-$RuSi_2$ phase at 75 GPa, the lattice parameters are a = 6.693 Å, b = 4.052 Å and c = 3.866 Å, where Ru atoms occupying the Wyckoff sites 4*c* (-0.500, 0.307, 0.750) are neighbored by equivalent Si atoms locating at 8*g* (-0.832, 0.316, 0.750) sites. More charmingly, the *Cmcm*-$RuSi_2$ phase contains two interpenetrating honeycomb-like silicon-layer along the c-axis, which forms the silicon hexagonal ring with one metal atom Ru located at the center of hexagonal ring in the *a*-*b* plane, disclosing that metallic atom and nonmetallic silicon layer are in the same flat. This layered feature is distinct from previously reported planar structures, such as MgB_2 [21], MoB_2 [22], NaC_2 [23], YC_2 [24], CeP_2 [28] and LaP_2 [29], where the hexagonal-ring nonmetallic layer and metallic atom generate two alternate layers and are distributed in different flats. In silicon hexagonal-ring, the there are two kinds of Si-Si bond lengths, corresponding to 2.298 and 2.461 Å, while the Si-Si bond length between the silicon layers is 2.456 Å. These three Si-Si bond lengths are elongated into 2.417, 2.668 and 2.655 Å, respectively, when the pressure decreases to the ambient pressure. Additionally, ten silicon atoms are coordinated around one Ru atom, forming a distorted $RuSi_{10}$ dodecahedron with four different Ru-Si bond lengths of 2.347, 2.431, 2.435 and 2.440 Å at 75 GPa, compared with the elongated Ru-Si bond separations of 2.523, 2.615, 2.554 and 2.683 Å under atmospheric pressure. Both of Si-Si and Ru-Si bond distances provide an explanation of the Si-Si and Ru-Si covalent bonds in the *Cmcm*-$RuSi_2$ crystal at ambient pressure and high pressure, which can also be substantiated by the electron localization in the intermediate regions of the Si-Si and Ru-Si bonds, as depicted in Figures 3(c), 3(d), 3(e) and 3(f). In short, based on the overall analyses of bond length and ELF, the *Cmca*-$RuSi_2$ and *Cmcm*-$RuSi_2$ phases under ambient pressures as well as the *Cmcm*-$RuSi_2$ phase under high pressure are characterized by a combination of the covalent Ru-Si and Si-Si bonds.

Preprints.org (www.preprints.org) | NOT PEER-REVIEWED | Posted: 7 October 2024 doi:10.20944/preprints202410.0466.v1

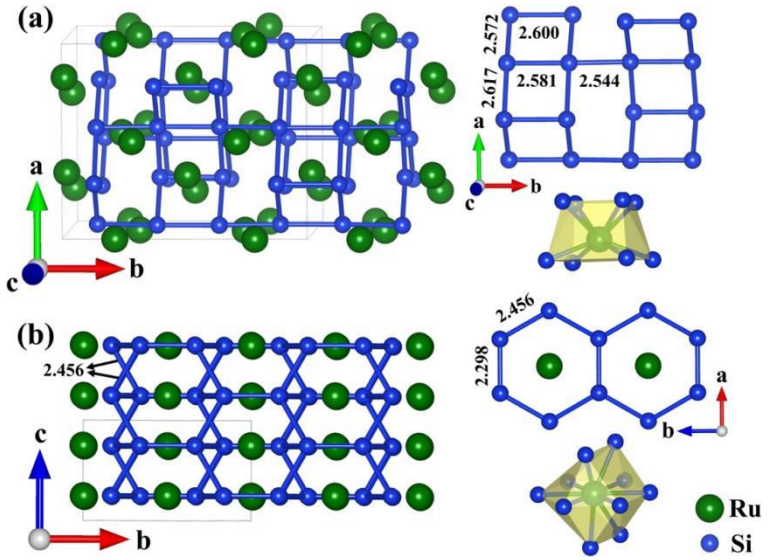

Figure 2. Crystal structures of two stable $RuSi_2$ phases. The green and blue spheres represent Ru and Si atoms, respectively. (a) *Cmca*-$RuSi_2$ at 1 atm, and (b) *Cmcm*-$RuSi_2$ at 75 GPa.

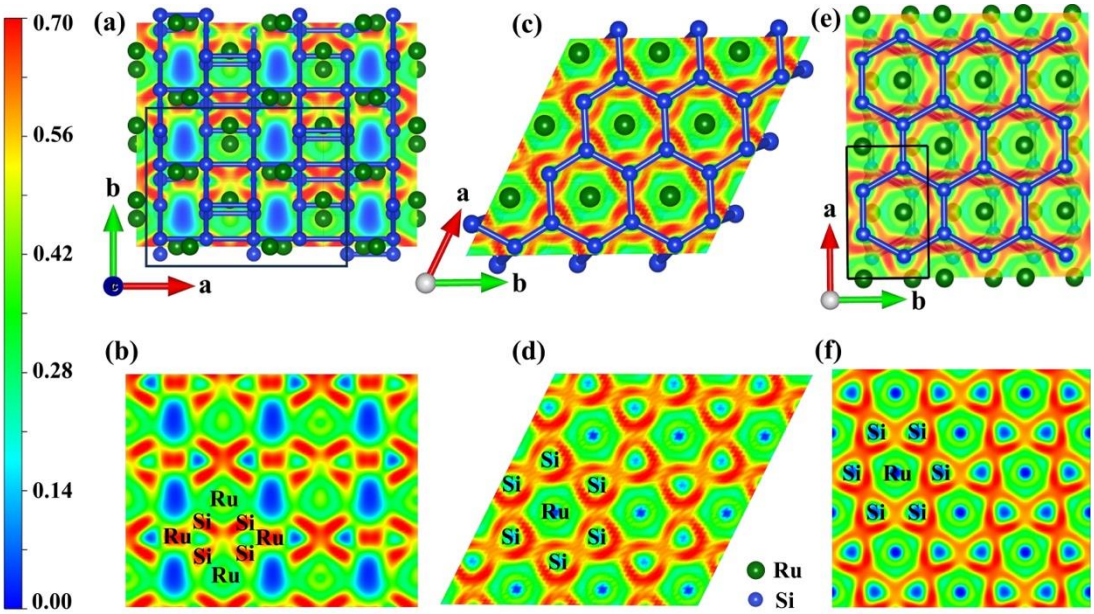

Figure 3. The 3D and 2D electron localization functions (ELF) of two stable $RuSi_2$ phases. (a) and (b) (001) plane for the *Cmca*-$RuSi_2$ at 1 atm, (c) and (d) (001) plane for the *Cmcm*-$RuSi_2$ at 1 atm, and (e) and (f) (001) plane for the *Cmcm*-$RuSi_2$ at 75 GPa. The green and blue spheres represent Ru and Si atoms, respectively.

The formation of strong covalent Ru–Si and Si–Si interactions in these two stable configurations of $RuSi_2$ can be quantitatively disclosed through the calculated crystal orbital Hamilton population (COHP) curves and integral crystal orbital Hamilton population (ICOHP) at the Fermi level, as displayed in Figure 4. The calculated ICOHP values for Ru–Si and Si–Si pairs in *Cmca*-$RuSi_2$ under 1 atm are –1.84 and –2.41 eV for per pair, respectively. Moreover, the predicted ICOHP values for the Ru–Si bonds in *Cmcm*-$RuSi_2$ at 1 atm and 75 GPa is –1.66 and –1.68 eV for per pair, respectively, with the corresponding ICOHP values of the Si–Si pairs –2.25 and –2.23 eV for per pair. Afterward, the predicted ICOHP values for the Si–Si pairs (–2.41, –2.25 and –2.23 eV for per pair) in both $RuSi_2$ structures are comparable to those of covalent Si–Si pairs in Na_4Si_{24} (–2.544 eV/pair) [76], P–P pairs in LaP_2 (–2.32 eV/pair) [29], P1–P2 pairs in Ce_2P_3 (–2.41 eV/pair) [28], B2–B2 pairs in LiB_4 (–2.55

 doi:10.20944/preprints202410.0466.v1

eV/pair) [79] and B2–B2 pairs in NaB_4 (–2.55 eV/pair) [80], reconfirming strong covalent Si–Si bond in both configurations. From the consequences above, it can be conspicuously found summarized into two aspects. On the one hand, the strength of the covalent Si–Si bond is stronger than that of the Ru–Si covalence in both $RuSi_2$ configurations as the estimated ICOHP values for the Si–Si pairs are slightly lower than those of the Ru–Si pairs. On the other hand, compared with the layered *Cmcm*-$RuSi_2$ phase, *Cmca*-$RuSi_2$ possesses the stronger Ru–Si and Si–Si covalent bonds, which should be the main driving force that the *Cmca*-$RuSi_2$ phase have more magnificent incompressibility than the *Cmcm*-$RuSi_2$ structure.

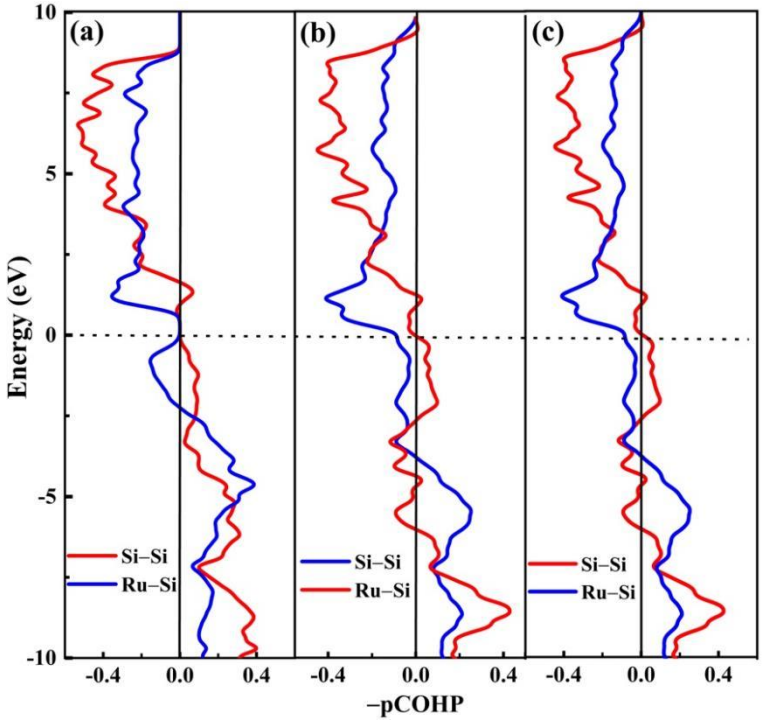

Figure 4. The crystal orbital Hamilton population (COHP) curves of two stable $RuSi_2$ phases. **(a)** *Cmca*-$RuSi_2$ at 1 atm, **(b)** *Cmcm*-$RuSi_2$ at 1 atm, and **(c)** *Cmcm*-$RuSi_2$ at 75 GPa. The dotted vertical line at 0 eV represents Fermi energy level.

3.3. Electronic Structure and Superconductive Property

To further delve into the electronic structures of the *Cmca*-$RuSi_2$ phase at 1 atm as well as the *Cmcm*-$RuSi_2$ phase at 1 atm and 75 GPa, we calculated their electronic band structure (BS) and density of states (DOS), as constructed in Figure 5. Note that the *Cmca*-$RuSi_2$ structure under ambient pressure displays a semiconductor behavior characterized by a direct band gap of 0.485 eV, in conformity with the preceding theoretical calculations reported by Zhang *et al* [49]. On the contrary, as the pressure increase, the conduction band and the valence band of *Cmcm*-$RuSi_2$ phase pass through the Fermi level (E_F) and overlap, implying its metallic character. In reality, a semiconductor-metal transformation or metallization occurs under high pressure, along with the structural transition from *Cmca*-$RuSi_2$ to *Cmcm*-$RuSi_2$. This phenomenon metallization induced by high pressure can also be appreciated in other systems, such as MgH_2 [81], $CaLi_2$ [82] and SiH_4 [83]. Moreover, the *Cmcm*-$RuSi_2$ phase still maintains the metallic characteristic when the pressure is released into the ambient pressure, as shown in Figure 5(b). On the other hand, the semi-conductive and metallic traits in *Cmca*-$RuSi_2$ and *Cmcm*-$RuSi_2$ can be elucidated in the right side of Figures 5(a), 5(b) and 5(c). On the basis of the total and partial density of states (TDOS and PDOS) of both $RuSi_2$ structures, it is obviously achieved that the Ru-4*d* state make the dominant contribution to TDOS. Apart form the Ru-4*d* state contribution, the Si-3*p* state also contributes to TDOS at a certain extent. The hybridization effect between the Ru-4*d* and Si-3*p* states near both sides of the E_F disclose the Ru-Si covalent bond in both $RuSi_2$ phases, which in excellent accord with the previous analyses of bond length, ELF, and COHP.

Preprints.org (www.preprints.org) | NOT PEER-REVIEWED | Posted: 7 October 2024 doi:10.20944/preprints202410.0466.v1

Eventually, the chemical bonding in the *Cmca*-$RuSi_2$ and *Cmcm*-$RuSi_2$ configurations comprises a complex combination of the covalent Ru-Si and Si-Si bonds with the Si-Si bond stronger than that of the Ru-Si bonding. More noticeably, as presented in the left sides of Figures 3(b) and 3(c), the electronic BS exhibits multiple characters in proximity to E_F, comprising of the hole pockets around *T*/*S*/*U* points, electron pockets around *Z*/*S* points and flat band along the *Y*-*S*-*X* direction. In view of the atypical BS, we further dig into the topological structure of Fermi surfaces (see Figure 6), which serve to unveil the electronic performance at the E_F. The emerge of three bands in *Cmcm*-$RuSi_2$ indicates excellent electrical conductivity and the third band should be attributed to the flat band along the *Y*-*S*-*X*, further secured by the decreased energy approaching the EF at the ambient pressure. These electronic traits proposed from the BS and Fermi surfaces have been comprehensively investigated and deemed as imperative signs for superconductivity.

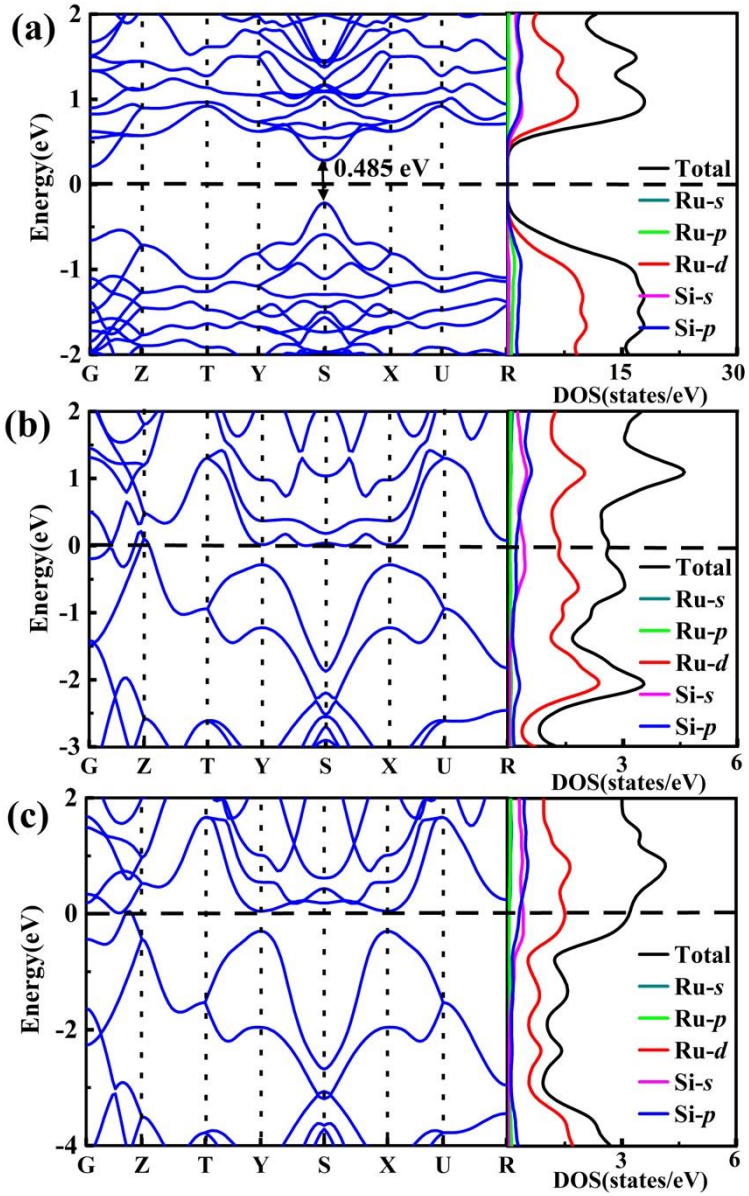

Figure 5. Electronic band structures and density of states (DOS) of two stable $RuSi_2$ phases. (**a**) *Cmca*-$RuSi_2$ at 1 atm, (**b**) *Cmcm*-$RuSi_2$ at 1 atm, and (**c**) *Cmcm*-$RuSi_2$ at 75 GPa.

 doi:10.20944/preprints202410.0466.v1

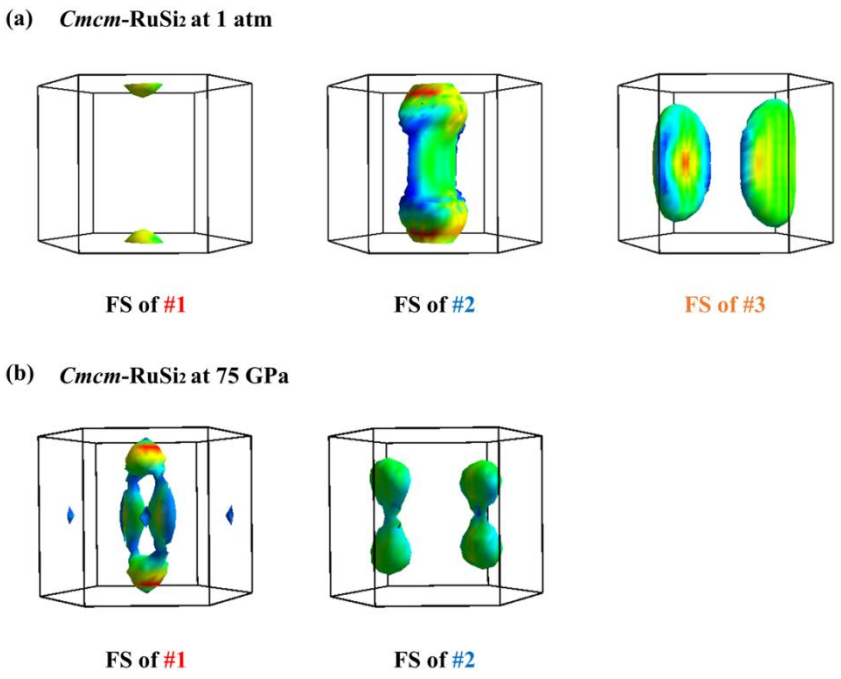

Figure 6. The nested Fermi surfaces for the *Cmcm*-$RuSi_2$ configuration at (**a**) 1atm and (**b**) 75 GPa.

Kindled by the metallic and significant band structure characters in *Cmcm*-$RuSi_2$ under ambient and high pressures coupled with the outstanding superconductivity in the layered framework in MgB_2 [21], MoB_2 [22], NaC_2 [23], KP_2 [27], CeP_2 [28], and LaP_2 [29] as well as alkali, alkaline-earth and rare-earth metal disilicides, analogous to the *Cmcm*-$RuSi_2$ phase, we assume that the layered *Cmcm*-$RuSi_2$ structure should be a promising superconductor. Subsequently, we calculated the phonon dispersion curves, the projected phonon density of states (PHDOS) and Eliashberg spectral function $\alpha^2F(\omega)$ together with the electron–phonon integral constant λ of *Cmcm*-$RuSi_2$ at 1 atm, 25 GPa, 50 GPa, and 75 GPa with the intention of illuminating their potential superconductivity, presented in Figure 7. As analysed above, its dynamical stability could be verified within the pressure range of 0–75 GPa as a consequence of the absence of imaginary phonon frequency throughout the whole Brillouin zone at 1 atm, 25 GPa, 50 GPa, and 75 GPa. In the PHDOS, the phonon vibrational modes of *Cmcm*-$RuSi_2$ can mainly be divided into three districts on the basis of the phonon region. The vibrations of Ru atoms mainly contribute to the low-frequency phonon regions (< 9 THz), while the high-frequency phonon modes (10–15 THz) are associated with silicon layers because of Ru atom heavier than Si atom. It is worthy noting that the intermediate-frequency branches stem from the coupled vibrations of Ru atom and Si layer. For the EPC parameter λ, the low-frequency vibrations by Ru atoms around below 9 THz contribute 82.4%, 77%, 74% and 67.5% at 1 atm, 25 GPa, 50 GPa and 75 GPa of the total λ, respectively, while the high-frequency phonon bands above 10 THz associated with light Si atom vibrations only account for 13.2%, 19.7%, 20.5% and 22.5% in *Cmcm*-$RuSi_2$, respectively. In addition, the corresponding coupled vibrations from Ru atoms and Si layer contribute 4.4%, 3.3%, 6.5% and 10% at 1 atm, 25 GPa, 50 GPa and 75 GPa of the total λ, respectively. This directly denotes that the vibrations from Ru atoms combined with the coupled vibrations between Ru atoms and Si layers play significant roles in the superconductivity of *Cmcm*-$RuSi_2$.

 doi:10.20944/preprints202410.0466.v1

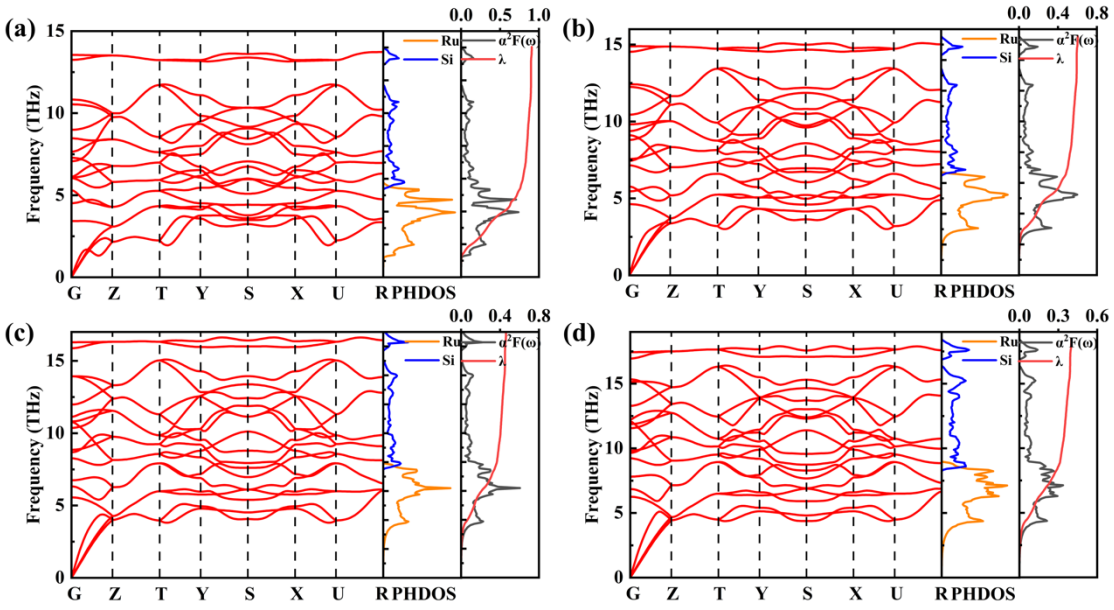

Figure 7. The phonon dispersion curves, the projected phonon density of states (PHDOS) and Eliashberg spectral function $\alpha^2F(\omega)$ together with the electron–phonon integral constants $\lambda(\omega)$ of (a) *Cmcm*-$RuSi_2$ at 1 atm, (b) *Cmcm*-$RuSi_2$ at 25 GPa, (c) *Cmcm*-$RuSi_2$ at 50 GPa, and (d) *Cmcm*-$RuSi_2$ at 75 GPa.

The electron-phonon coupling parameters λ, logarithmic average phonon frequency ω_{log}, electron density of states at the Fermi level $N(E_f)$ and superconducting transition temperature T_c of *Cmcm*-$RuSi_2$ at 1 atm, 25 GPa, 50 GPa and 75 GPa were also calculated in Table 1. The superconducting critical temperature T_c values are estimated by using the Allen–Dynes modified McMillan equation :

$$T_c = \frac{\omega_{\log}}{1.2}\exp\left[\frac{1.04(1+\lambda)}{\lambda-\mu^*(1+0.62\lambda)}\right]$$

where, the Coulomb pseudopotential parameters μ^* are set to typical 0.10 and 0.13, respectively. As summarized in Table 1, the predicted EPC parameter λ for the *Cmcm*-$RuSi_2$ crystal is 0.4 at 75 GPa and displays a monotonous decrease with the increment of the pressure. Accordingly, the maximal EPC parameter λ value of 0.91 emerges in *Cmcm*-$RuSi_2$ under ambient pressure, which is comparable to 0.93 for $RaSi_2$ at 0 GPa, 1.1 for $CaSi_2$ at 0 GPa, 0.92 for Al_2Si_3 at 10 GPa, 1.01 for *P*6_3/*mmc*-Y_3Si, but larger than 0.81 for *P*6/*mmm*-$MgSi_3$ at 0 GPa, 0.808 for *Cmmm*-Si_4 at ambient pressure, 0.897 for *P*6/*m*-$NaSi_6$ at 0 GPa, 0.799 *P*6/*m*-Si_6 at 0 GPa. To compare with the former binary conventional superconductors, we draw a overall diagram which displays a combination of the T_c and stabilized pressure for established superconductors, as shown in Figure 8. Additionally, the detailed T_c values

For the conventional superconductors at different pressures are summarized in Table S3. It is undoubtedly found that the *Cmcm*-$RuSi_2$ structure are estimated to be 10.07 K at atmospheric pressure, which is comparable to 13.7 K in $MgSi_3$, 13 K in *P*6/*m*-$NaSi_6$ and 12 *P*6/*m*-Si_6 at 0 GPa, 14 K for $CaSi_2$ at 15 GPa, 10.5 K for *P*6/*mmm*-CeP_2 at 16.5 GPa, and 13.6 K for CrB_2 at 60.7 GPa, but higher than other transition metal disilicides, such as $RbSi_2$ (9 K) [34], $MgSi_2$ (~7 K) [35,36], $BaSi_2$ (6.8 K) [39], $LaSi_2$ (2.5 K) [40] and YSi_2 (0.5 K, 50 GPa) [41]. In short, the novel *Cmcm*-$RuSi_2$ configuration at ambient pressure possesses the secondarily highest T_c among the binary metal disilicides, merely lower than that of $CaSi_2$ (14 K) under 15 GPa. In addition, it is worthy mentioning that the superconducting critical temperature T_c in *Cmcm*-$RuSi_2$ is significantly higher than those of the corresponding metallic *Cmcm*-Si_4 (2.2 K) [87] and Ru (0.51 K) [91,92] at ambient pressure, which tremendously advance the superconductivity for the related elemental substances.

The investigation of the variation trends with the increasing pressure serve as an appropriate pathway for a deeper understanding of the superconductivity driven in *Cmcm*-$RuSi_2$, as intuitively

 doi:10.20944/preprints202410.0466.v1

exhibited Figure 9. Regarding the broad stable pressure range obtained in *Cmcm*-$RuSi_2$, we have implemented calculations to estimate its pressure-dependent superconductivity. As the pressure decreases, a successive increase presents in the T_c values, eventually reaching 10.07 K at atmospheric pressure. Manifestly, two substantial parameters (λ and ω_{log}) play a vital role in determining T_c, displaying the contrasting trends with pressure. The increment in T_c with decreasing pressure results from the synchronous enhancement in λ, which dominates the evolution of T_c with pressure. The growth in λ should be related to the increasing DOS at the Fermi energy upon the reducing pressure, which further originate from the decrease of charges of Ru-4*d* orbital transferred from silicon layer, as tabulated in Table S4. In the *Cmcm*-$RuSi_2$ phase, one Ru atom gain 1.38 *e* at 75 GPa and reduces to 1.06 *e* under ambient pressure. The charge transferred from nonmetallic Si to metallic Ru is feasible for the reason that the electronegativity value of Si (1.90) element is lower than that of Ru element according to the periodic table of the elements. The anion character in metallic element Ru is rarely seen in binary metal silicides. In contrast, the reducing process of ω_{log} with the decreasing pressure should be attributed to the elongation of Si–Si bonds within the configuration. Upon the reducing compression, the variation trend of λ (increment) and ω_{log} (diminution) is similar to those in Ce_2P_3, CeP_2 [28]and Sc_2P [93].

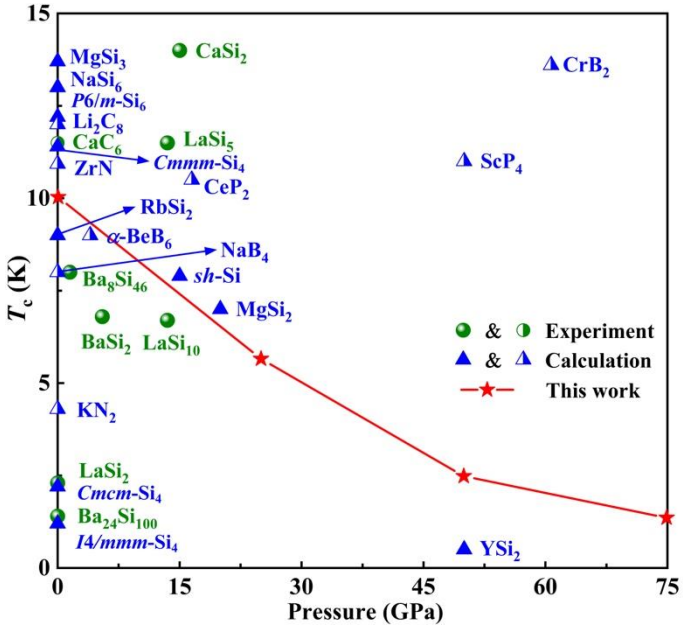

Figure 8. Pressure dependence of T_c values for typical superconductors. The green filled and half-filled circles stand for the T_c values of well-known metal silicides and other binary compounds in experiment, respectively [9-11,32,38-40,84]. The blue filled and half-filled triangles denote the T_c values of well-known metal silicides and other binary compounds in theory, respectively [25,33,35,41,43,85-90]. The red filled stars the T_c values (μ^* = 0.1) of the *Cmcm*-$RuSi_2$ configuration at four different pressures.

Preprints.org (www.preprints.org) | NOT PEER-REVIEWED | Posted: 7 October 2024 doi:10.20944/preprints202410.0466.v1

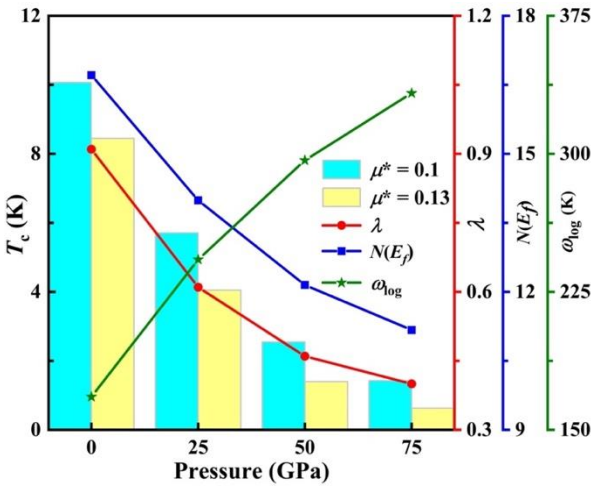

Figure 9. Calculated electron-phonon coupling parameters λ, electronic density of states at the Fermi level $N(E_f)$ (states/spin/Ry/Unit Cell), logarithmic average phonon frequency ω_{log} (K), and superconducting transition temperature T_c (K) in *Cmcm*-$RuSi_2$ phase as a function of pressure with μ^* = 0.10 and 0.13.

Table 1. Calculated electron-phonon coupling parameters λ, electronic density of states at the Fermi level $N(E_f)$ (states/spin/Ry/Unit Cell), logarithmic average phonon frequency ω_{log} (K), and superconducting transition temperature T_c (K) of *Cmcm*-$RuSi_2$ at 1 atm, 25 GPa, 50 GPa and 75 GPa, respectively.

Structure	Pressure	ω_{log}	$N(E_f)$	λ	T_c	
					$\mu^* = 0.10$	$\mu^* = 0.13$
Cmcm-$RuSi_2$	1 atm	167.97	16.71	0.91	10.07	8.45
	25 GPa	242.56	13.99	0.61	5.71	4.05
	50 GPa	296.50	12.15	0.46	2.55	1.40
	75 GPa	332.95	11.17	0.40	1.43	0.63

As the representative superconductor in the component of 1:2 in binary metallic compounds, MgB_2 encompasses a similar honeycomb B layer, differing from *Cmcm*-$RuSi_2$. It is necessary to unlock the discrepancy in the structural characters, electronic properties, the superconducting mechanism and T_c values between both phases at ambient pressure. In regard to the structural trait, the honeycomb B layer and Mg atoms are located in the alternate layers along the *c* axis in MgB_2 whereas the graphene-like Si layer and the Ru atoms are in the same plane with Ru atom sited at the center of the Si hexatomic ring. In the case of the metallic character, MgB_2 mainly stems from the B-2*p* orbital while the current *Cmcm*-$RuSi_2$ should be ascribed to the Ru-4*d* state. The high frequency for MgB_2 derives from the graphene-like B layer with the superconductivity of MgB_2 dominated by the electron-phonon coupling of B atoms [94], while the transition Ru-4*d* orbital electrons also take part in the coupling. This comparison not only points toward a possibility to uncover different superconducting sources in the traditional prototype phases, such as H_3S, CaH_6 and LaH_{10}, but also widens the cognition of the elemental contributions in superconductivity. As for the T_c value, MgB_2 is higher than *Cmcm*-$RuSi_2$, which can be summarized as the following reasons: (a) The MgB_2 has an open B layer without the B–B interlayer covalence while *Cmcm*-$RuSi_2$ contains an closed Si layer with the interlayer covalent Si–Si bond; (b) the bond strength of Si-Si bond in *Cmcm*-$RuSi_2$ is weaker than that of MgB_2, as demonstrated by the calculated ICOHP (–2.25 per pair Si–Si in comparison with –6.92 per pair B–B); (c) the ω_{log} value for *Cmcm*-$RuSi_2$ is lower than that of MgB_2 (167.97 K with respect to 450 K) [94], which results from the lower phonon frequencies of Ru and Si atoms lower than those of Mg and B atoms, as related to the larger atomic mass of Ru and Si, respectively.

 doi:10.20944/preprints202410.0466.v1

3.4. Mechanical Property and Hardness

With the high development in the superconductor, it necessitates the eminent mechanical property and hardness integrated with spectacular ductility. The elastic constants for the *Cmca*-$RuSi_2$ and *Cmcm*-$RuSi_2$ phases at 1 atm in conjunction with the *Cmcm*-$RuSi_2$ configuration under ambient pressure and 75 GPa were computed through the identical strain−stress means [95], as corroborated in Table 2. Both phases are dynamically stable under focused pressures as they satisfy the mechanical stability criteria for the orthorhombic crystal system [96]. Thereafter, the homologous shear modulus *G*, bulk modulus *B*, *B*/*G*, Young's modulus *E* and Poisson's ratio *ν* of both phases can be attainable from the elastic constants based on the Voigt–Reuss–Hill (VRH) method [97] (see Table 2). In the *Cmca*-$RuSi_2$ configuration under ambient pressure, the current estimated elastic constants C_{ij}, bulk modulus *B*, shear modulus *G*, Young's modulus E and Poisson's ratio *v* are in conformity with the prior theoretical consequens [49], clarifying that the methodology utilized in present work is convincing. Generally speaking, the C_{11}, C_{22} and C_{33} values in material denote the resistance to compression along the corresponding *a*-, *b*- and *c*-axis. From Table 2, *Cmcm*-$RuSi_2$ under 75 GPa possesses ultra-high C_{11}, C_{22} and C_{33} values, which are much higher than those of *P*6/*mmm*-ScB_2 [98], explaining that this phase behaves excellent incompressibility along *a*-, *b*- and *c*-axis. The calculated *B*, *G* and *E* values of *Cmcm*-$RuSi_2$ under 75 GPa are 410.13, 184.99 and 482.44 GPa, respectively, which are significantly higher than those of the *Cmca*-$RuSi_2$ phase at ambient pressure (*B*, *G* and *E* values are 173.53 , 107.99 and 268.30 GPa, respectively), corroborating that this phase transition induced by compression enhances the mechanical properties of $RuSi_2$ crystal to a great extent. Moreover, the value of *B*/*G* can estimate the brittle or ductile manner of a solid: a high ratio of *B*/*G* (> 1.75) indicates the ductility, while a low ratio (< 1.75) indicates the brittleness according to the Pugh criterion [99,100]. For transition metal silicides, the improvement of ductility can greatly improve their industrial work efficiency, because their actual productionS as high-temperature materials are limited by their own brittleness [101-103]. As listed in Table 2, the the *B*/*G* value of *Cmca*-$RuSi_2$ at 1 atm is 1.61, uncovering the brittle nature whereas the *B*/*G* values of *Cmcm*-$RuSi_2$ at 1 atm and 75 GPa are 2.03 and 2.22, corresponding to ductile character, respectively. This phenomenon confirms the brittle-to-ductile transformation in $RuSi_2$, accompanied by the structural transformation under high pressure, which is analogous to $NbSi_2$ [104] and MoN_2 [105].

Table 2. Elastic constants C_{ij} (GPa), shear modulus *G* (GPa), bulk elastic modulus *B* (GPa), *B*/*G*, Young's modulus *E* (GPa) and Poisson's ratio *ν* of two stable $RuSi_2$ structures.

Pressure	Space group	C_{11}	C_{22}	C_{33}	C_{44}	C_{55}	C_{66}	C_{12}	C_{13}	C_{23}	*G*	*B*	*B*/*G*	*E*	*ν*
1 atm	*Cmca*	271	336	327	103	111	122	115	90	112	107.99	173.53	1.61	268.30	0.24
1 atm	*Cmcm*	389	288	292	85	90	69	96	112	128	89.28	181.20	2.03	230.05	0.29
75 GPa	*Cmcm*	836	676	594	149	173	188	261	246	298	184.99	410.13	2.22	482.44	0.30

Hardness should be characterized as a substantial mechanical property of a material and can be used to measure the ability to resist local deformation, especially plastic deformation, indentation or scratches. In addition, the orientation bond in a material is an important index to measure its hardness, and it can be expressed by Pugh's ratio *G*/*B* [99,100]. A larger *G*/*B* value corresponds to a higher hardness. As summarized in Table 2, the *G*/*B* values of *Cmca*-$RuSi_2$ and *Cmcm*-$RuSi_2$ phases under atmospheric pressure are 0.64 and 0.49, respectively. However, Gao *et al*. indicated that the vital problem in digging into the hardness of materials is how to describe the strength of internal bonds of the materials. Thus, we further probe into the hardness values of both structures employing the hardness model proposed by Gao et al [106,107]. The Vickers hardness could be calculated with the following formula:

$$H_v = \{\prod^{\mu}[740P^{\mu}(V_b^{\mu})^{-\frac{5}{3}}]^{n^{\mu}}\}^{\frac{1}{\sum n^{\mu}}}$$

 doi:10.20944/preprints202410.0466.v1

where

$$V_b^{\mu} = (d^{\mu})^3 / \sum [(d^{v})^3 N_b^{\mu}]$$

where μ labels all different types of covalent bonds in the system, P^{μ} is the Mulliken overlap population of the μ type bond, v_b^{μ} is its volume, n^{μ} is the number of μ type bonds, d^{μ} is its bond length, and N_b^{μ} is the bond number of type μ per unit volume. On account of the aforementioned empirical equation, the estimated hardness values of *Cmca*-$RuSi_2$ and *Cmcm*-$RuSi_2$ phases reach 31.74 and 26.76 GPa, respectively (see Table 3). The hardness value of *Cmca*-$RuSi_2$ under ambient pressure is consistent with the previous theoretical results [49]. The predicted H_v values of *Cmca*-$RuSi_2$ (31.74 GPa) and *Cmcm*-$RuSi_2$ (26.76 GPa) are comparable to the experimental measurements of β-SiC (34 GPa) [106], BP (33 GPa) [108], TiC (32 GPa) [109] β-Si_3N_4 (30 GPa) [109] and transition metal disilicide WSi_2 (28.5 GPa) [110], but higher than elemental solid Si (12 GPa) [106]. Hence, it can be concluded that both *Cmca*-$RuSi_2$ and *Cmcm*-$RuSi_2$ are potential high hardness materials. In comparison with *Cmcm*-$RuSi_2$, *Cmca*-$RuSi_2$ has a higher hardness, which can be ascribed to the stronger Ru–Si and Si–Si covalent bonds and better orientation than those of *Cmcm*-$RuSi_2$.

Table 3. Calculated bond parameters and Vickers hardness H_v (GPa) of two stable structures.

	bond	*P*	*n*	*d* (Å)	V_b (Å^3)	H_v (GPa)
Cmca	Ru-Si	0.38	16	2.452	2.955	31.7
		0.30	16	2.458	2.977	28[a]
		0.35	16	2.460	2.984	
		0.41	16	2.460	2.986	
		0.36	16	2.467	3.010	
		0.30	16	2.484	3.072	
		0.30	16	2.500	3.131	
		0.27	16	2.523	3.219	
	Si-Si	0.33	8	2.541	3.289	
		0.32	16	2.570	3.402	
		0.28	8	2.576	3.428	
		0.27	8	2.598	3.514	
		0.31	16	2.612	3.574	
		0.18	8	2.689	3.898	
		0.20	16	2.693	3.913	
Cmcm	Ru-Si	2.23	8	2.226	6.367	26.8
		0.32	4	2.242	6.513	
	Si-Si	0.37	4	2.293	6.967	
[a] Reference [49].		0.76	4	2.307	7.095	

4. Conclusions

To sum up, our comprehensive first-principles structure searches in $RuSi_2$ within the pressure range of 0–300 GPa have disclosed the emerge of the peculiar *Cmcm*-$RuSi_2$ phase at 50.97 GPa. This *Cmcm*-$RuSi_2$ configuration contain an extraordinary graphene-like silicon layer, which is dynamically stable and simultaneously leads to exceptional superconductivity and high hardness under ambient pressure, despite it is recovered from the high pressure. On the one hand, its predicted T_c value could reach 10.07 K at ambient pressure, comparable to the previous proposed *P*6/*m*-$NaSi_6$ (13 K) and $CaSi_2$(14 K)。 On the other hand, the Vickers hardness value is 26.76 GPa, which is comparable to WSi_2 (28.5 GPa). Furthermore, its excellent conductivity stem from the the strong interaction between Ru-4*d* electrons and the phonons B–B and coupled Ru–Si vibrations, while its high hardness can be ascribed to the 3D robust Ru–Si and Si–Si directional covalent framework. In addition, the *Cmcm*-

 doi:10.20944/preprints202410.0466.v1

$RuSi_2$ phase is a ductile material. The ambient-pressure ground *Cmca* phase is a narrow-gap semiconductor with a estimated hardness of 31.7 GPa.

The special graphene-like silicon layer in the transition-metal disilicides *Cmcm*-$RuSi_2$ phase broaden the existing silicon-layer space beyond alkali, alkaline-earth and rare-earth metal disilicides. The removal of metal atoms can be utilized to acquire silicon framework such as layered silicon, silicon clathrates and other silicon allotropes. This mode has uncovered a succession of novel elemental structures, such as *I*4/*mmm*-B_4, *Pm*-B_{17} [80] and *P*6/*m*-Si_6 [33], which is destined to promote the quest for the analogous silicon laminar structures and distinct silicon motifs (eg. 3D silicon clathrate framework and 1D silicon chains) in elemental silicon and transition-metal silicides. On the other hand, this layered network in *Cmcm*-$RuSi_2$ provide a wonderful bedding for adding light element adatoms to layered superconductors, which could enhance the superconductivity for the parent *Cmcm*-$RuSi_2$ configuration. This method has been practically employed recently to improve the superconductivity in very diverse ultrathin materials, ranging from monolayer MgB_2 to truly 2D atomic sheets doped graphene and transition metal dichalcogenides.

The *Cmcm*-$RuSi_2$ structure has the secondarily highest superconducting transition temperature among the metal disilicides, MSi_2 (M = metal), merely lower than that of $CaSi_2$ (14 K), which facilitate the in-depth investigation on the superconductivity mechanism in the metal disilicides in both theory and experiment.

The anion transition-metal in *Cmcm*-$RuSi_2$ is rarely reported in preceding binary compounds that contains metal and nonmetal elements, which widens the physical and chemical cognition.

Supplementary Materials: The following supporting information can be downloaded at the website of this paper posted on Preprints.org., Figure S1: Nine structures of $RuSi_2$ at ambient pressure. The red and green spheres represent Ru and Si atoms, respectively; Figure S2: The phonon dispersion curves of *Cmca*-$RuSi_2$ at ambient pressure.

Author Contributions: Supervision, C.Z., Y.J. and W.S.; Formal analysis, K.G. and W.S.; Investigation, C.Z. and Y.W.; Writing, C.Z. and Y.W.; Review and editing, Y.J. and W.S.; Calculation, Y.W., M.L., F.Y. and W.S.; Visualization, Y.W., M.L. and F.Y.; Funding acquisition, K.G. and Y.J. All authors have read and agreed to the published version of the manuscript.

Funding: This work was supported by the National Key Research and Development Program of China (No. 2023YFB3712300), National Natural Science Foundation of China (11804031), Key Science and Technology Foundation of Gansu Province (No. 22JR5RA095) and 'Light of West China' Program of CAS.

Institutional Review Board Statement: Not applicable.

Informed Consent Statement: Not applicable.

Data Availability Statement: Data are contained within the article and Supplementary Information.

Conflicts of Interest: The authors declare no conflict of interest.

References

1. Wang, H.; Tse, J.S.; Tanaka, K.; Iitaka, T.; Ma, Y. Superconductive sodalite-like clathrate calcium hydride at high pressures. *Proc. Natl. Acad. Sci. USA* **2012**, *109*, 6463-6466.
2. Ma, L.; Wang, K.; Xie, Y.; Yang, X.; Wang, Y.; Zhou, M.; Liu, H.; Yu, X.; Zhao, Y.; Wang, H.; Liu, G.; Ma, Y. High-temperature superconducting phase in clathrate calcium hydride CaH_6 up to 215 K at a pressure of 172 GPa. *Phys. Rev. Lett.* **2022**, *128*, 167001.
3. Du, M.; Li, Z.; Duan, D.; Cui, T. Superconducting phases of YH_9 under pressure. *Phys. Rev. B* **2023**, *108*, 174507.
4. Kong, P.; Minkov, V.S.; Kuzovnikov, M.A.; Drozdov, A.P.; Besedin, S.P.; Mozaffari, S.; Balicas, L.; Balakirev, F.F.; Prakapenka, V.B.; Chariton, S.; Knyazev, D.A.; Greenberg, E.; Eremets, M.I. Superconductivity up to 243 K in the yttrium-hydrogen system under high pressure. *Nat. Commun.* **2021**, *12*, 5075.
5. Errea, I.; Belli, F.; Monacelli, L.; Sanna, A.; Koretsune, T.; Tadano, T.; Bianco, R.; Calandra, M.; Arita, R.; Mauri, F.; Flores-Livas, J.A. Quantum crystal structure in the 250-kelvin superconducting lanthanum hydride. *Nature* **2020**, *578*, 66-69.
6. Geballe, Z.M.; Liu, H.; Mishra, A.K.; Ahart, M.; Somayazulu, M.; Meng, Y.; Baldini, M.; Hemley, R.J. Synthesis and stability of lanthanum superhydrides. *Angew. Chem. Int. Ed.* **2018**, *57*, 688-692.

7. Zhong, X.; Sun, Y.; Iitaka, T.; Xu, M.; Liu, H.; Hemley, R.J.; Chen, C.; Ma, Y. Prediction of above-room-temperature superconductivity in lanthanide/actinide extreme superhydrides. *J. Am. Chem. Soc.* **2022,** *144*, 13394-13400.
8. Li, Z. ; He, X. ; Zhang, C. ; Lu, K. ; Min, B.; Zhang J.; Zhang, S.; ZhaoJ.; Shi, L.; Peng, Y.; Feng, S.; Deng, Z.; Song, J.; Liu, Q.; Wang, X.; Yu, R.; Wang, L.; Li, Y.; Bass, J.D.; Prakapenka, V.; Chariton, S.; Liu, H.; Jin, C.; Sci. Superconductivity above 70 K observed in lutetium polyhydrides. *China Phys. Mech.* **2023**, *66*, 267411.
9. Yamanaka, S.; Enishi, E.; Fukuoka, H.; Yasukawa, M. High-Pressure synthesis of a new silicon clathrate superconductor, Ba_8Si_{46}. *Inorg. Chem.* **2000**, *39*, 56-58.
10. Imai, M.; Kikegawa, T. In situ observation of the formation of Si clathrate Ba_8Si_{46} at high pressure and high temperature. *Inorg. Chem.* **2008**, *47*, 8881-8883.
11. Gao, K.; Cui, W.; Chen, J.; Wang, Q.; Hao, J.; Shi, J.; Liu, C.; Botti, S.; Marques, M.A.L.; Li, Y.; Superconducting hydrogen tubes in hafnium hydrides at high pressure. *Phys. Rev. B* **2021**, *104*, 214511.
12. Liu, M.; Cui, W.; Shi, J.; Hao, J.; Li, Y. Superconducting H7 chain in gallium hydrides at high pressure. *Phys. Chem. Chem. Phys.* **2023**, *25*, 7223-7228.
13. Li, X.; Guo, Z.; Zhang, X.; Yang, G. Layered hydride LiH_4 with a pressure-insensitive superconductivity. *Inorg. Chem.* **2024**, *63*, 8257-8263.
14. Zhou, D.; Jin, X.; Meng, X.; Bao, G.; Ma, Y.; Liu, B. and Cui, T.; *Ab* initio study revealing a layered structure in hydrogen-rich KH_6 under high pressure. *Phys. Rev. B.* **2012**, *86*, 0147118.
15. Wang, Y.; Chen, S.; Guo, J.; Huang, X.; Cui, T. Absence of superconductivity in *I*4/*mmm*-FeH_5: experimental evidence. *Phys. Chem. Chem. Phys.* **2024**, *26*, 7371-7376.
16. Xie, H.; Yao, Y.; Feng, X.; Duan, D.; Song, H.; Zhang, Z.; Jiang, S.; Redfern, S.A.T.; Kresin,V. Z.; Pickard, C. J.; Cui, T. Hydrogen pentagraphenelike structure stabilized by hafnium: a high-temperature conventional superconductor. *Phys. Rev. Lett.* **2020**, *125*, 217001.
17. Chen, Y.; Liu, Z.; Lin, Z.; Jiang, Q.; Du, M.; Zhang, Z.; Song, H.; Xie, H.; Cui, T.; Duan, D. High T_c superconductivity in layered hydrides XH_{15} (X = Ca, Sr, Y, La) under high pressures. *Front. Phys.* **2022**, *17*, 103-109.
18. Jiang, Q.; Chen, L.; Du, M.; Duan, D. A perspective on reducing stabilizing pressure for high-temperature superconductivity in hydrides. *J. Phys.: Condens. Matter* **2024**, *36*, 493002.
19. Song, J.; Curtin, W.A. Atomic mechanism and prediction of hydrogen embrittlement in iron curtin, *Nat. Mater*. **2013**, *12*, 145-151.
20. Dwivedi, S.K.; Vishwakarma, M. Hydrogen embrittlement in different materials: A review. *Int. J. Hydrogen Energ.* **2018**, *43*, 21603-21616.
21. Nagamatsu, J.; Nakagawa, N.; Muranaka, T.; Zenitani, Y.; Akimitsu, J. Superconductivity at 39 K in magnesium diboride. *Nature*, **2001**, *410*, 63-64.
22. Pei, C.; Zhang, J.; Wang, Q.; Zhao, Y.; Gao, L.; Gong, C.; Tian, S.; Luo, R.; Li, M.; Yang, W.; Lu, Z.Y.; Lei, H.; Liu, K.; Qi, Y. Pressure-induced superconductivity at 32 K in MoB_2. *Natl. Sci. Rev*. **2023**, *10*, nwad034.
23. Yang, Q.; Zhao, K.; Liu, H.; Zhang, S. Superconductive sodium carbides with pentagon carbon at high pressures. *J. Phys. Chem. Lett.* **2021**, *12*, 5850-5856.
24. Feng, X.; Lu, S.; Pickard, C.J.; Liu, H.; Redfern, S.A.T.; Ma, Y. Carbon network evolution from dimers to sheets in superconducting ytrrium dicarbide under pressure. *Commun. Chem.* **2018**, *1*, 85.
25. Yang, Q.; Zhao, Y.; Jiang, X ; Wang, B.; Zhao, J.; Mater, J. Unconventional stoichiometric two-dimensional potassium nitrides with anion-driven metallicity and superconductivity. *Chem. C* **2024**, *12*, 103-109.
26. Chen, Y.; Cai, X.; Wang, H.; Wang, H.; Wang, H. Novel triadius-like N_4 specie of iron nitride compounds under high pressure. *Sci. Rep.* **2018**, *8*, 10670.
27. Liu, Y.; Wang, C.; Kong, X.; Duan, D. Stability and superconductivity of K–P compounds under Pressure. *Inorg. Chem.* **2017**, *56*, 12529-12534.
28. Li, X.; Bergara, A.; Zhang, X.; Li, F.; Liu, Y.; Yang, G. Superconducting Ce_2P_3 and CeP_2 with an interesting planar P layer. *J. Mater. Chem. C* **2024**, *12*, 2526-2533.
29. Li, X.; Zhang, X.; Yang, Z.; Liu, Y.; Yang, G. Pressure-stabilized graphene-like P layer in superconducting LaP_2. *Phys. Chem Chem. Phys.* **2022**, *24*, 6469-6475.
30. Connétable, D.; Timoshevskii, V.; Masenelli, B.; Beille, J.; Marcus, J.; Barbara, B.; Saitta, A.M.; Rignanese, G.-M. Superconductivity in doped sp^3 semiconductors: the case of the clathrates. *Phys. Rev. Lett.* **2003**, *91*, 247001.
31. Rachi, T.; Yoshino, H.; Kumashiro, R.; Kitajima, M.; Kobayashi, K.; Yokogawa, K.; Murata, K.; Kimura, N.; Aoki, H.; Fukuoka, H.; Yamanaka, S.; Shimotani, H.; Takenobu, T.; Iwasa, Y.; Sasaki, T.; Kobayashi, N.; Miyazaki, Y ; Saito, K.; Guo, F.; Kobayashi, K.; Osaka, K.; Kato, K.; Takata, M,; Tanigaki1, K. Superconductivity and physical properties of $Ba_{24}Si_{100}$ determined from electric transport, specific-heat capacity, and magnetic susceptibility measurements. *Phys. Rev. B* **2005**, *72*, 144504.
32. Yamanaka, S.; Izumi, S.; Maekawa, S.; Umemoto, K. Phase diagram of the La–Si binary system under high pressure and the structures of superconducting $LaSi_5$ and $LaSi_{10}$. *J. Solid. State. Chem.* **2009**, *182*, 1991-2003.

33. Sung, H.-J.; Han, W.H.; Lee, I.-H.; Chang, K.J. Superconducting open-framework allotrope of silicon at ambient pressure. *Phys. Rev. Lett.* **2018**, *120*, 157001.
34. Flores-Livas, J.A ; Sanna, A. Spintronics: Superconductivity in intercalated group-IV honeycomb structures. *Phys. Rev. B*. **2015**, *91*, 054508.
35. Huan, T.D. Spintronics: Pressure-stabilized binary compounds of magnesium and silicon. *Phys. Rev. Mater*. **2018**, *2*, 023803.
36. Zha, D.-B.; Jiang, P.; Huang, H.-M.; Li, Y.-L. Spintronics: Refined phase diagram and kagome-lattice superconductivity in Mg-Si system. *Phys. Rev. Mater*. **2023**, *7*, 114805.
37. Bordet, P.; Affronte, M.; Sanfilippo, S.; Nunez-Regueiro, M.; Laborde, O.; Olcese, G.L.; Palenzona, A.; LeFloch, S.; Levy, D.; Hanfland, M. Spintronics: Structural phase transitions in under high pressure. *Phys. Rev. B*. **2000**, *62*, 11392-11397.
38. Sanfilippo, S.; Elsinger, H.; Nunez-Regueiro, M.; Laborde, O.; LeFloch, S.; Affronte, M.; Olcese, G.L.; Palenzona, A. Spintronics: Superconducting high pressure $CaSi_2$ phase with T_c up to 14 K. *Phys. Rev. B*. **2000**, *61*, R3800-R3803.
39. Imai, M.; Hirata, K.; Hirano, T. Spintronics: Superconductivity of trigonal $BaSi_2$ *Physica C*. **1995**, *245*, 12-14.
40. Satoh, T.; Asada, Y.J. Spintronics: Superconductivity of $LaSi_2$. *Phys. Soc. Japan*. **1970**, *28*, 263-263.
41. Zhang, J.; Chen, G.; Liu, H. Spintronics: Stable structures and superconductivity in a Y-Si system under high pressure. *J. Phys. Chem. Lett*. **2021**, *12*, 10388-10393.
42. Hilleke, K.P.; Zurek, E. Rational Design of Superconducting Metal Hydrides via Chemical Pressure Tuning. *Angew. Chem. Int. Ed*. **2022**, *61*, e202207589.
43. Flores-Livas, J.A.; Debord, R.; Botti, S.; Miguel, A.S.; Pailhès, S.; Marques, M.A.L. Spintronics: Superconductivity in layered binary silicides: A density functional theory study. *Phys. Rev. B*. **2011**, *84*, 184503.
44. Buschinger, B.; Geibel, C.; Diehl, J.; Weiden, M.M.; Guth, W.; Wildbrett, A.; Horn, S.; Steglich, F. Spintronics: Preparation and low temperature properties of FeSi-type RuSi. *J. Alloy. Compd*. **1997**, *256*, 57-60.
45. Perring, L.; Bussy, F.; Gachon, J.C.; Feschotte, P. The ruthenium-silicon system. *J. Alloy. Compd.* **1999**, *284*, 198-205.
46. Opahle, I.; Madsen, G.K.H.; Drautz, R. High throughput density functional investigations of the stability, electronic structure and thermoelectric properties of binary silicides. *Phys. Chem. Chem. Phys.* **2012**, *14*, 16197-16202.
47. Wolf, W.; Bihlmayer, G.; Blügel, S. Electronic structure of the Nowotny chimney-ladder silicide Ru_2Si_3. *Phys. Rev. B* **1997**, *55*, 6918-6926.
48. Ivanenko, L.; Behr, G.; Spinella, C.R.; Borisenko, V.E. $RuSi_2$: evidence of a new binary phase in the ruthenium-silicon system. *J. Cryst. Growth* **2002**, *236*, 572-576.
49. Zhang, C.; Kuang, X.; Jin, Y.; Lu, C.; Zhou, D.; Li, P.; Bao, G.; Hermann, A. Prediction of stable ruthenium silicides from first-principles calculations: stoichiometries, crystal structures, and physical properties. *ACS Appl. Mater. Inter.* **2015**, *7*, 26776-26782.
50. Xiong, Z.; Wang, X.; Cao, L.; Wang, J.; Yu, J.; Yin, H.; Wang, X.; Ma, J. Structural stability, phase transition, electronic, elastic and thermodynamic properties of RuX (X= Si, Ge, Sn) alloys under high pressure. *J. Alloy. Compd.* **2017**, *693*, 440-447.
51. Ivanenkoa, L.I.; Shaposhnikova, V.L.; Filonova, A.B.; Krivosheevaa, A.V.; Borisenkoa, V.E.; Migasb, D.B.; Migliob, L.; Behrc, G.; Schumannc, J. Electronic properties of semiconducting silicides: fundamentals and recent predictions. *Thin solid films* **2004**, *461*, 141-147.
52. Zhang, L.; Wang, Y.; Lv, J.; Ma, Y. Materials discovery at high pressures. *Nat. Rev. Mater.* **2017**, *2*, 1-16.
53. Miao, M.; Sun, Y.; Zurek, E.; Lin, H. Chemistry under high pressure. *Nat. Rev. Chem.* **2020**, *4*, 508-527.
54. Wang, Y.; Lv, J.; Zhu, L.; Ma, Y. Crystal structure prediction via particle-swarm optimization. *Phys. Rev. B* **2010**, *82*, 094116.
55. Wang, Y.; Lv, J.; Zhu, L.; Ma, Y. CALYPSO: A method for crystal structure prediction. *Comput. Phys. Commun.* **2012**, *183*, 2063-2070.
56. Wang, W.; Zhang, C.; Jin, Y.; Li, S.; Zhang, W.; Kong, P.; Xie, C.; Du, C.; Liu, Q.; Zhang, C. Structural, mechanical and electronic properties and hardness of ionic vanadium dihydrides under pressure from first-principles computations. *Sci. Rep.* **2020**, *10*, 8868.
57. Wang, Y.; Jin, Y.; Yang, F.; Zhang, J.; Zhang, C.; Kuang, F.; Ju, M.; Li, S.; Cheng, S. Prediction of potential high-temperature superconductivity in ternary Y-Hf-H compounds under high pressure. *Sci. Rep.* **2024**, *14*, 17670.
58. Jin, Y.; Huang, W.; Zhang, J.; Li, S.; Cheng, S.; Sun, W.; Ju, M.; Zhang, C. An unexpectedly stable Y_2B_5 compound with the fractional stoichiometry under ambient pressure. *Arab. J. Chem.* **2023**, *16*, 104546.
59. Wang, Y.; Zhang, C.; Zhang, J.; Li, S.; Ju, M.; Sun, W.; Dou, X.; Jin, Y. A ten-fold coordinated high-pressure structure in hafnium dihydrogen with increasing superconducting transition temperature induced by enhancive. *Chinese Phys. B* **2023**, *32*, 527-534.

60. Becke, A.D.; Edgecombe, K.E. A simple measure of electron localization in atomic and molecular systems. *J. Chem. Phys.* **1990**, *92*, 5397-5403.
61. Savin, A.; Jepsen, O.; Flad, J.; Andersen, O.K.; Preuss, H.; Schnering, H.G. Electron localization in solid-state structures of the elements: the diamond structure. *Angew. Chem., Int. Ed. Engl.* **1992**, *31*, 187-188.
62. Kresse, G.; Furthmüller, J. Efficient iterative schemes for *ab initio* total-energy calculations using a plane-wave basis set. *Phys. Rev. B* **1996**, *54*, 11169-11186.
63. Perdew, J.P.; Burke, K.; Ernzerhof, M. Generalized gradient approximation made simple.*Phys. Rev. Lett.* **1996**, *77*, 3865-3868.
64. Perdew, J.P.; Chevary, J.A.; Vosko, S.H.; Jackson, K.A.; Pederson, M.R.; Singh, D.J.; Fiolhais, C. Atoms, molecules, solids, and surfaces: Applications of the generalized gradient approximation for exchange and correlation. *Phys. Rev. B* **1992**, *46*, 6671.
65. Kresse, G.; Joubert, D. From ultrasoft pseudopotentials to the projector augmented-wave method. *Phys. Rev. B.* **1999**, *59*, 1758-1775.
66. Monkhorst, H.J.; Pack, J.D. Special points for brillouin-zone integrations. *Phys. Rev. B* **1976**, *13*, 5188-5192.
67. Dronskowski, R.; Bloechl, P.E. Crystal orbital Hamilton populations (COHP): energy-resolved visualization of chemical bonding in solids based on density-functional calculations. *J. Phys. Chem*. **1993**, *97*, 8617-8624.
68. Maintz, S.; Deringer, V.L.; Tchougréeff, A.L.; Dronskowski, R. LOBSTER: A tool to extract chemical bonding from plane-wave based DFT. *J. Comput. Chem.* **2016**, *37*, 1030-1035.
69. Giannozzi, P.; Baroni, S.; Bonini, N.; Calandra, M.; Car, R.; Cavazzoni, C.; Ceresoli, D.; Chiarotti, G.L.; Cococcioni, M.; Dabo, I.; Corso, A.D.; Gironcoli, S.; Fabris, S.; Fratesi, G.; Gebauer, R.; Gerstmann, U.; Gougoussis, C.; Kokalj, A.; Lazzeri, M.; Martin-Samos, L.; Marzari, N.; Mauri, F.; Mazzarello, R.; Paolini, S.; Pasquarello, A.; Paulatto, L.; Sbraccia, C.; Scandolo, S.; Sclauzero, G.; Seitsonen, A.P., Smogunov, A.; Umari, P.; Wentzcovitch, R.M. QUANTUM ESPRESSO: a modular and open-source software project for quantum simulations of materials. *J. Phys.: Condens. Matter* **2009**, *21*, 395502.
70. Opahle, I.; Parma, A.; McEnary, E.J.; Drautz, R.; Madsen, G.KH. High-throughput study of the structural stability and thermoelectric properties of transition metal silicides. *New J. Phys*. **2013**, *15*, 105010.
71. Siegrist, T.; Hulliger, F.; Travaglini, G. The crystal structure and some properties of $ReSi_2$. *J. Alloy. Compd.* **1983**, *92*, 119-129.
72. Cynn, H.; Klepeis, J.E.; Yoo, C.S.; Young, D.A. Osmium has the lowest experimentally determined compressibility. *Phys. Rev. Lett.* **2002**, *88*, 135701.
73. Shen, G.; Ikuta, D.; Sinogeikin, S.; Li, Q.; Zhang, Y.; Chen, C. Direct observation of a pressure-induced precursor lattice in silicon. *Phys. Rev. Lett.* **2012**, *109*, 205503.
74. Vocado, L.; Price, G.D.; Wood, I.G. Crystal structure, compressibility and possible phase transitions in ε-FeSi studied by first-principles pseudopotential calculations. *Acta Cryst*. **1999**, *B55*, 484-493.
75. Shaposhnikov, V.L.; Filonov, A.B.; Krivosheeva, A.V.; Ivanenko, L.I.; Borisenko, V.E. Structural, electronic and optical properties of a new binary phase–ruthenium disilicide. *Phys. Stat. Sol. (b)* **2005**, *242*, 2864-2871.
76. Kim, D.Y.; Stefanoski, S.; Kurakevych, O.O.; Strobel, T.A. Synthesis of an open-framework allotrope of silicon. *Nat. Mater.* **2015**, *14*, 169-173.
77. Pan, Y.; Jing, C.; Wu, Y. The structure, mechanical and electronic properties of WSi_2 from first-principles investigations. *Vacuum* **2019**, *167*, 374-381.
78. Wang, J.; Kuang, X.; Jin, Y.; Lu, C.; Huang, X. Theoretical investigation on the structural phase transition, elastic properties and hardness of RhSi under high pressure. *J. Alloy Compd.* **2014**, *592*, 42-47.
79. Wang, Q.; Li, H.; Wei, J.; Zhong, T.; Zhu, L.; Zhang, X.; Liu, H.; Zhang, S. Hardness and superconductivity in tetragonal LiB_4 and NaB_4. *J. Chem. Phys.* **2023,** *159*, 234707.
80. Zhang, S.; Du, X.; Lin, J.; Bergara, A.; Chen, X.; Liu, X.; Zhang, X.; Yang, G. Superconducting boron allotropes. *Phys. Rev. B.* **2020,** *101*, 174507.
81. Zhang, C.; Sun, G.; Wang, J.; Lu, C.; Jin, Y.; Kuang, X.; Hermann, A. Prediction of novel high-pressure structures of magnesium niobium dihydride. *ACS Appl. Mater. Interfaces* **2017,** *9*, 26169-26176.
82. Matsuoka, T.; Debessai, M.; Hamlin, J.J.; Gangopadhyay, A.K.; Schilling, J.S. Pressure-Induced superconductivity in $CaLi_2$. *Phys. Rev. Lett.* **2008,** *100*, 197003.
83. Chen, X.-J.; Wang, J.-L.; Struzhkin, V.V.; Mao, H.; Hemley, R.J.; Lin, H.-Q. Superconducting behavior in compressed solid with a layered structure. *Phys. Rev. Lett.* **2008,** *101*, 077002.
84. Weller, T.E.; Ellerby, Mark.; Saxena, S.S.; Smith, R.P.; Skipper, N.T. Superconductivity in the intercalated graphite compounds C_6Yb and C_6Ca *Nat. Phys*. **2005**, *1*, 39-41.
85. Yang, Q.P.; Zhang, H.M.; Zhao, J.J.; Jiang, X. Probing the superconductivity limit of Li-doped graphene. *Adv. Funct. Mater.* **2024**, 2406023.
86. Liao, Z.W.; Yi, X.W.; You, J.Y.; Gu, B.; Su, G. Family of binary transition metal pnictide superconductors. *Phys. Rev. B* **2023**, *108*, 014501.

87. Kang, Y.-Gu.; Lee, I.-H.; Han, M.J.; Chang, K.J. Spintronics: Ab initio prediction of nontrivial topological band and superconductivity in stable metallic Si allotropes at ambient pressure. *Phys. Rev. Mater.* **2021**, *5*, 104802.
88. Wu, L.L.; Wan, B.; Liu, H.Y.; Gou, H.Y.; Yao, Y.S.; Li, Z.P.; Zhang, J.W.; Gao, F.M.; Mao, H-k. Spintronics: Coexistence of superconductivity and superhardness in beryllium hexaboride driven by inherent multicenter bonding. *J. Phys. Chem. Lett*. **2016**, *7*, 4898−4904.
89. Fu, Y.; Li, F.; Zhang, X.H.; Zhang, S.L.; Liu,Y.; Yang, G.C. Superconducting ScP_4 with a novel phosphorus framework. *Appl. Phys. A* **2022**, 128:318.
90. Sananda, B.; Kreisel, A.; Valadkhani, A.; Dürrnagel, M.; Schwemmer, T.; Thomale, R.; Valentí, R.; Mazin, I.I. Hybrid *s*-wave superconductivity in CrB_2. *Phys. Rev. B* **2023**, L020501.
91. Schilling, J. S. Studies in superconductivity at extreme pressures. *Physica C* **2007**, *460*, 182-185.
92. Hamlin, J.J. Superconductivity in the metallic elements at high pressures. *Physica C* **2015**, *514*, 59-76.
93. Zhao, K.; Wang, Q.; Li, H.; Gao, B.; Wei, S.; Zhu, L.; Xu, H.; Liu, H.; Zhang, S. Superconductivity in dense scandium-based phosphides. *Phys. Rev. B* **2023**, *108*, 174513.
94. Kortus, J.; Mazin, I.I.; Belashchenko, K.D.; Antropov, V.P.; Boyer, L.L. Superconductivity of Metallic Boron in MgB_2. *Phys. Rev. Lett.* **2001**, *86*, 4656-4659.
95. Lu, C.; Kuang, X.Y.; Wang, S.J.; Zhao, Y.R.; Tan, X.M. Theoretical investigation on the high-pressure structural transition and thermodynamic properties of cadmium. *Europhys. Lett.* **2010**, *91*, 16002.
96. Mouhat, F.; Coudert, F.X. Necessary and sufficient elastic stability conditions in various crystal systems. *Phys. Rev. B* **2014**, *90*, 224104.
97. Connétable, D.; Thomas, O. First-principles study of the structural, electronic, vibrational, and elastic properties of orthorhombic NiSi. *Phys. Rev. B* **2009**, *79*, 094101.
98. Shein, I.R.; Ivanovskii, A.L. Elastic properties of mono-and polycrystalline hexagonal AlB_2-like diborides of *s*, *p* and *d* metals from first-principles calculations. *J. Phys.: Condens. Matter* **2008**, *20*, 415218.
99. Wu, Z.J.; Zhao, E.J.; Xiang, H.P.; Hao, X.F.; Liu, X.J.; Jian, M. Crystal structures and elastic properties of superhard IrN_2 and IrN_3 from first principles. *Phys. Rev. B* **2007**, *76*, 054115.
100. Haines, J.; Léger, J.M.; Bocquillon, G. Synthesis and design of superhard materials. *Annu. Rev. Mater. Res.* **2001**, *31*, 1-23.
101. Pan, Y.; Wang, S.L.; Zhang, X.; Jia, L.H. First-principles investigation of new structure, mechanical and electronic properties of Mo-based silicides. *Ceram. Int.* **2018**, *44*, 1744-1750.
102. Todai, M.; Hagihara, K.; Kishida, K.; Inui, H.; Nakano, T. Microstructure and fracture toughness in boron added $NbSi_2$ (C40)/$MoSi_2$ (C11b) duplex crystals. *Scr. Mater.* **2016**, *113*, 236-240.
103. Zhang, G.H.; Sun, G.D.; Chou, K.C. A novel process to prepare $MoSi_2$ by reaction between MoS_2 and Si. *J. Alloy Compd.* **2017**, *694*, 480-488.
104. Pu, D.L.; Pan, Y. Influence of high pressure on the structure, hardness and brittle-to-ductile transition of $NbSi_2$ ceramics. *Ceram. Int.*, **2021**, *47*, 2311-2318.
105. Ding, L.P.; Shao, P.; Zhang, F.H.; Lu, C.; Huang, X.F. Prediction of molybdenum nitride from first-principle calculations: crystal structures, electronic properties, and hardness. *J. Phys. Chem. C* **2018**, *122*, 21039-21046.
106. Gao, F.M.; He, J.L.; Wu, E.D.; Liu, S.M.; Yu, D.L.; Li, D.C.; Zhang, S.Y.; Tian, Y.J. Hardness of covalent crystals. *Phys. Rev. Lett.* **2003**, *91*, 015502.
107. Gao, F.M. Theoretical model of intrinsic hardness. *Phys. Rev. B* **2006**, *73*, 132104.
108. Andrievski, R.A. Superhard materials based on nanostructured high-melting point compounds: achievements and perspectives. *Int. J. Refract. Met. Hard Mater.* **2001**, *19*, 447-452.
109. Guo, X.J.; Li, L.; Liu, Z.Y.; Yu, D.L.; He, J.L.; Liu, R.P.; Xu, B.; Tian, Y.J.; Wang, H.T. Hardness of covalent compounds: Roles of metallic component and d valence electrons. *J. Appl. Phys.* **2008**, *104*, 023503.
110. Yan, H.Y.; Wei, Z.T.; Zhang, M.G.; Wei, Q. Exploration of stable stoichiometries, ground-state structures, and mechanical properties of the W-Si system. *Ceram. Int.* **2020**, *46*, 17034-17043.